The Journal of Chemical Physics

RESEARCH ARTICLE | MARCH 10 2026

Open-boundary molecular dynamics of red blood cell suspensions

Special Collection: Festschrift in honor of Kurt Kremer: Computational Polymer Science and Soft Matter Physics

Maša Lah ; Tilen Potisk ; Matej Praprotnik

J. Chem. Phys. 164, 104107 (2026)
https://doi.org/10.1063/5.0313643

The Journal of Chemical Physics ARTICLE pubs.aip.org/aip/jcp

Open-boundary molecular dynamics of red blood cell suspensions

Cite as: J. Chem. Phys. 164, 104107 (2026); doi: 10.1063/5.0313643
Submitted: 24 November 2025 • Accepted: 25 February 2026 •
Published Online: 10 March 2026

Maša Lah,[1,2] Tilen Potisk,[1,2] and Matej Praprotnik[1,2,3,a)]

AFFILIATIONS

[1] Laboratory for Molecular Modeling, National Institute of Chemistry, SI-1001 Ljubljana, Slovenia
[2] Department of Physics, Faculty of Mathematics and Physics, University of Ljubljana, SI-1000 Ljubljana, Slovenia
[3] Universitat de Barcelona Institute of Complex Systems, 08028 Barcelona, Spain

Note: This paper is part of the JCP Festschrift in Honor of Kurt Kremer.
[a)]**Author to whom correspondence should be addressed:** praprot@cmm.ki.si

ABSTRACT

Blood is a complex suspension of deformable red blood cells (RBCs), and its rheology plays a central role in physiology and pathology. While many computational studies have examined hemorheology under periodic or wall-confined flows, these approaches cannot capture the exchange of mass, momentum, and energy with the surroundings, a feature essential for the realistic simulation of non-equilibrium processes. Open-boundary methods provide this capability but remain largely underexplored. We present the first application of open-boundary molecular dynamics (OBMD) to RBC suspensions, with explicit control of flux exchange across the open boundary. The framework combines dissipative particle dynamics for the solvent and a coarse-grained RBC membrane model and introduces a novel, efficient membrane insertion algorithm capable of handling high hematocrits. It reproduces experimental bulk hemorheological properties, including shear-thinning and hematocrit-dependent viscosity. Our results validate OBMD for modeling blood rheology and establish a computational foundation for future studies of ultrasound–blood interactions and other phenomena where periodic boundaries constrain natural dynamics, such as pressure-driven flows, transient inflows, and cell-free layer formation.

I. INTRODUCTION

Blood is a complex suspension of cells. Its macroscopic flow properties are governed primarily by red blood cells (RBCs), accounting for more than 95% of the cellular content.[1] The deformability of RBC membranes and hematocrit, which describes the volume percentage of RBCs in blood, strongly influence the apparent viscosity of blood. Alterations in either of these properties are closely linked to pathology. For example, malaria-infected RBCs stiffen and increase their resistance to flow, while in sickle cell disease, cells adopt an abnormal shape with decreased deformability. Hematocrit can also vary widely, ranging from as low as 10% in severe anemia to over 60% in polycythemia.[1] Moreover, the viscosity of a single blood sample is strongly shear-dependent, varying over orders of magnitude across the shear rates encountered in the circulation. A long history of experimental work has established the dependence of blood viscosity on both shear rate and hematocrit.[1–3]

Capturing such behavior requires cell-resolved simulations capable of reproducing both the nonlinear rheology of bulk blood and the heterogeneous microstructures that arise in flow. Among mesoscale methods, dissipative particle dynamics (DPD),[4–14] lattice Boltzmann methods,[15–17] and smoothed particle hydrodynamics[12,18–20] have been applied to study RBC deformation, aggregation, and suspension rheology. These methods have been successful in reproducing many aspects of blood flow;[4–23] however, they rely on periodic boundary conditions (PBCs) to approximate bulk behavior. PBCs are efficient, since simulating macroscopic systems is computationally prohibitive, but they are not suitable for non-equilibrium conditions. They impose artificial synchronization at the boundaries and require continuous external forcing, such as moving walls or Lees–Edwards-type boundary conditions,[24] to sustain steady or oscillatory flows. In contrast, real flows are maintained through ongoing mass and momentum exchange with the surroundings. The challenge of representing such an exchange has motivated

the development of hybrid and open-boundary schemes that explicitly control fluxes across the simulation boundaries. Early work by Flekkøy *et al.*[25,26] introduced hybrid continuum–MD schemes and established the formalism for flux exchange between particle and continuum regions. Delgado-Buscalioni *et al.*[27–29] implemented these ideas, with overlapping buffer regions for transmitting continuum boundary conditions to the particle domain, and extended the approach to triple-scale simulations, imposing shear flow via external walls and treating the MD region as an open system through flux exchange and adaptive-resolution particle insertion. Further studies by Fedosov and Karniadakis[30] introduced the triple-decker framework, coupling continuum, DPD, and MD domains to simulate multiscale hydrodynamics. More recently, Lykov *et al.*[31] developed a particle-based method for non-periodic blood flow simulations, in which RBC inflow is replicated from a PBC simulation and the outflow is regulated by adaptive forces.[32]

The open-boundary molecular dynamics (OBMD) method,[33] which is used to simulate the particle domain of the triple-scale scheme mentioned above, has been applied to complex soft matter systems such as sheared star-polymer melts[34] and ultrasound propagation in water[35,36] and used to study the excitation of protein vibrational modes.[37] OBMD combines adaptive resolution (AdResS)[28] with open MD,[26,38] using external forces on the outer layers of the system to control flux exchange while the bulk dynamics remain fully governed by Newton's equations of motion. While OBMD has demonstrated success in simulating complex systems, it has not yet been applied to densely packed cell suspensions.

In this work, we extend OBMD to heterogeneous RBC suspensions and introduce a novel growing-size insertion algorithm that enables simulations at high hematocrit. The simulation box is divided into predefined regions, similar to AdResS,[28] but instead of interpolating resolutions as in AdResS or temporally scaling interactions as in FADE,[39] our method gradually increases the effective packing density. RBC membranes are inserted at a reduced size and smoothly grown to full dimensions as they traverse the boundary region toward the bulk. This allows cells to deform and rearrange while entering the dense suspension. Similar procedures, in which the size grows with time, are commonly used to generate the initial configuration for densely packed systems,[15,40,41] but spatially growing sizes have, to the best of our knowledge, never before been used to enable insertions of large objects into the system. We model the solvent and cytosol as DPD fluids, and RBC membranes as triangulated surfaces with node forces derived from continuum theory. Our approach maintains uniform density in the region of interest under equilibrium and reproduces experimental hemorheological behavior. By validating this computational framework, we provide a foundation for simulating RBC suspensions under acoustic forcing, which requires physically consistent mass and momentum exchange at domain boundaries.

II. MODELS AND METHODS

A. Dissipative particle dynamics

Dissipative particle dynamics (DPD)[42] is a mesoscopic particle-based method that is used widely in the soft matter community to model complex systems such as blood,[4–7] polymers,[43] and colloids,[44] and it has already been used together with OBMD.[35–37] Each DPD particle represents a group of molecules that interacts with other particles within a cutoff range with three central pairwise forces. Importantly, DPD conserves the overall linear momentum and recovers the Navier–Stokes equations in the continuum limit. The equations of motion for a DPD particle of mass m_i are

$$m_i \frac{\mathrm{d}\boldsymbol{v}_i}{\mathrm{d}t} = \sum_{j\neq i} \boldsymbol{F}_{ij}^C + \boldsymbol{F}_{ij}^R + \boldsymbol{F}_{ij}^D, \qquad \frac{\mathrm{d}\boldsymbol{r}_i}{\mathrm{d}t} = \boldsymbol{v}_i, \tag{1}$$

where

$$\boldsymbol{F}_{ij}^C = a w(r_{ij}) \hat{\boldsymbol{e}}_{ij}, \tag{2}$$

$$\boldsymbol{F}_{ij}^R = \sigma w_R(r_{ij}) \Theta_{ij} \hat{\boldsymbol{e}}_{ij}, \tag{3}$$

$$\boldsymbol{F}_{ij}^D = -\gamma w_D(r_{ij}) (\boldsymbol{v}_{ij} \cdot \hat{\boldsymbol{e}}_{ij}) \hat{\boldsymbol{e}}_{ij} \tag{4}$$

are the conservative, random, and dissipative forces exerted by bead j on bead i, respectively. Here, $\boldsymbol{v}_{ij} = \boldsymbol{v}_i - \boldsymbol{v}_j$ and $\boldsymbol{r}_{ij} = \boldsymbol{r}_i - \boldsymbol{r}_j$ are the relative velocity and displacement of the particle pair, respectively, $\hat{\boldsymbol{e}}_{ij} = \boldsymbol{r}_{ij}/r_{ij}$, and $r_{ij} = |\boldsymbol{r}_{ij}|$. The stochastic contribution is introduced with Θ_{ij}, a Gaussian white noise variable that is symmetric in particle indices ($\Theta_{ij} = \Theta_{ji}$) with zero mean and unit variance. The force contributions are modulated by the following three weight functions: $w(r)$ for the conservative force, $w_R(r)$ for the random one, and $w_D(r)$ for the dissipative force. Their respective amplitudes are controlled by parameters a, σ, and γ. The random and dissipative forces together act as the thermostat, determining the temperature of the system T through the dissipation–fluctuation theorem,

$$\sigma^2 = 2\gamma k_B T, \tag{5}$$

where k_B is the Boltzmann constant. The weight functions satisfy

$$w_D(r) = [w_R(r)]^2 = [w(r)]^{2s}, \tag{6}$$

where s controls the effective friction between the particles, here set as $s = 0.125$. The weight function is defined as

$$w(r) = \begin{cases} 1 - r/r_c, & r < r_c, \\ 0, & r \geq r_c, \end{cases} \tag{7}$$

with a cutoff distance r_c. The equation of state for a DPD fluid is

$$p = \rho k_B T + \alpha r_c^4 a \rho^2, \tag{8}$$

where ρ is the number density and $\alpha \approx 0.101$ is an empirical parameter.[42]

B. Open-boundary molecular dynamics

To simulate an open system, we use OBMD,[33] which combines the principles of open MD,[26,38] allowing momentum and mass transfer across the system's boundaries, and AdResS,[28] which can be used for the insertion of complex objects into the system. Instead of AdResS, we use the growing-size insertion algorithm here (see Sec. II B 2). While AdResS is effective for objects such as star polymers,[34] RBCs present additional challenges due to their closed membrane structure and high packing densities. Even slight overlaps can lead to "locked" configurations, but the growing-size approach

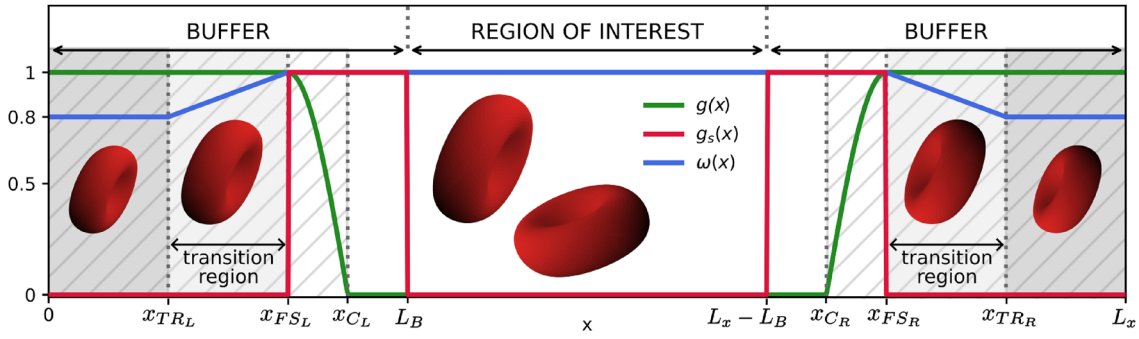

FIG. 1. In OBMD, the simulation box is divided into two buffer regions of length L_B and the central region of interest. The outer surface is open, and the particles are free to diffuse out of the box. External forces are distributed only to the particles in the buffer according to the weighting functions $g(x)$ and $g_s(x)$. In simulations with high-hematocrit, the cells are inserted at a fraction of their size in equilibrium (here, $\omega_0 = 0.8$). Their size, controlled by the weighting function $\omega(x)$, grows smoothly in the transition region. The striped regions denote the regions where the bounce-back reflection is disabled. In low-hematocrit simulations, where the cells are inserted at their full size, no reduced-size and transition regions are needed.

allows cells to deform as they expand, which prevents overlaps and enables high packing fractions.

In OBMD, the simulation box is split into three regions, as shown in Fig. 1. The central region of interest (ROI) serves as the primary simulation region, where particles move according to the standard equations of motion, Eq. (1). The simulation box is open in one spatial direction (usually along the x-axis) and periodic in the orthogonal directions (y- and z-axes). The method can, in principle, be generalized to different types of geometries and dimensions,[45] for example, to configurations that are open in two or three spatial directions, where flux exchange over a closed surface (cylindrical or spherical, respectively) is considered.[46,47] For most applications, however, periodicity in the lateral directions provides an efficient and practical compromise for approximating bulk behavior. At the two open edges, we introduce buffer layers that serve both as particle reservoirs and flux-exchanging regions. The number of particles in each buffer is kept approximately constant with a simple feedback algorithm $\Delta N = \Delta t/\tau_B(N_0 - N)$, where Δt is the time step, τ_B is the buffer relaxation time usually set to $\tau_B \approx 100\,\Delta t$, and N_0 and N are the desired and current number of particles in the buffer, respectively. If $\Delta N > 0$, new particles will be inserted into the buffer with the USHER[48] algorithm that performs energy minimization on the potential energy surface. When a particle crosses the open boundary, it is deleted from the simulation.

To impose boundary conditions, we apply external forces $\boldsymbol{f}_i^{ext}$ to particles in the buffers. They are designed so that the total linear momentum across the whole particle system is conserved and are determined by considering the momentum balance at the open edge,

$$\boldsymbol{J}A\cdot\hat{\boldsymbol{n}} = \sum_{i\in B}\boldsymbol{f}_i^{\mathrm{ext}} + \frac{1}{\Delta t}\sum_{i'}\Delta(m_{i'}\boldsymbol{v}_{i'}), \tag{9}$$

where $\boldsymbol{J}$ is the momentum flux tensor, A is the surface area of the buffer-ROI interface, and $\hat{\boldsymbol{n}}$ is the inward unit normal to that interface. The index i runs over all particles in the buffer, while i' runs over all the particles that were inserted or deleted in the previous time step. For an inserted particle, the momentum change is $\Delta(m_{i'}\boldsymbol{v}_{i'}) = m_{i'}\boldsymbol{v}_{i'}$, and for a deleted particle it is $\Delta(m_{i'}\boldsymbol{v}_{i'}) = -m_{i'}\boldsymbol{v}_{i'}$. The momentum flux across the boundary is controlled by

$$\boldsymbol{J}A\cdot\hat{\boldsymbol{n}} = p_{xx}A\hat{\boldsymbol{n}} + p_{xy}A\hat{\boldsymbol{t}}, \tag{10}$$

where p_{xx} and p_{xy} are the normal and shear stress contributions, respectively, and $\hat{\boldsymbol{t}} = \pm\hat{\boldsymbol{e}}_y$. The external forces are distributed among the buffer particles based on their mass and position,

$$\boldsymbol{f}_i^{\mathrm{ext}} = G(x_i)\left[p_{xx}A\hat{\boldsymbol{n}} - \frac{1}{\Delta t}\sum_{i'}\Delta(m_{i'}\boldsymbol{v}_{i'})\right] + G_s(x_i)p_{xy}A\hat{\boldsymbol{t}}, \tag{11}$$

where $G(x)$ and $G_s(x)$ are the general and shear stress distribution functions defined as

$$G(x_i) = \frac{g(x_i)m_i}{\sum_{j\in B}g(x_j)m_j}, \quad G_s(x_i) = \frac{g_s(x_i)m_i}{\sum_{j\in B}g_s(x_j)m_j}, \tag{12}$$

with the weighting functions $g(x)$ and $g_s(x)$,

$$g(x) = \begin{cases} 1, & x \le x_{FS_L}, \\ \cos\left(\dfrac{\pi}{2}\dfrac{x - x_{FS_L}}{x_{C_L} - x_{FS_L}}\right), & x_{FS_L} < x < x_{C_L}, \\ 0, & x_{C_L} \le x \le x_{C_R}, \\ \sin\left(\dfrac{\pi}{2}\dfrac{x - x_{C_R}}{x_{FS_R} - x_{C_R}}\right), & x_{C_R} < x < x_{FS_R}, \\ 1, & x \ge x_{FS_R}, \end{cases} \tag{13}$$

$$g_s(x) = \begin{cases} 1, & x_{FS_L} \le x \le L_B \text{ or } L_x - L_B \le x \le x_{FS_R}, \\ 0, & \text{otherwise}, \end{cases}$$

where we set $x_{C_L} = (L_B + x_{FS_L})/2$ and $x_{C_R} = (L_x - L_B + x_{FS_R})/2$; see Fig. 1. The function $g(x)$ is smooth, whereas $g_s(x)$ is a step function. This choice is motivated by the fact that $g(x)$ acts in the direction of density gradients. A smooth ramp in $g(x)$ ensures gradual adaptation to the low-density region. In contrast, $g_s(x)$ acts tangentially along directions of nearly constant density, so a smoothing ramp is not needed.

1. Red blood cells in the open framework

Depending on the simulation setup, the RBC insertion algorithm can be applied at different levels of complexity. Under equilibrium conditions, RBCs are not expected to leave the computational domain. Their thermal diffusion coefficient can be estimated using the Stokes–Einstein relation,

$$D = \frac{k_B T}{6\pi\eta_s R}, \tag{14}$$

which assumes an isolated spherical particle in a Newtonian fluid but provides an upper bound for the actual diffusivity of a RBC. For $R = 3.9\ \mu$m, $k_B T \approx 4.16 \times 10^{-21}$ J, and $\eta_s \approx 1.2$ mPa s, this yields $D \sim 4.7 \times 10^{-14}$ m^2 s^{-1}. The corresponding diffusion time over one cell radius is $t \sim R^2/6D \approx 56$ s, exceeding the simulation duration. Their thermal diffusion is, therefore, negligible, and RBC motion is mainly dominated by flow. No feedback or reinsertion is usually required under equilibrium or steady shear flow, where flow is imposed perpendicular to the open boundaries. During the initial OBMD equilibration phase, however, transient oscillations in density and momentum occur as the system relaxes toward steady state. The initial imbalance between inflow and outflow generates a pressure wave where particles first stream out of the domain and are then reintroduced by the insertion mechanism. In this phase, RBC membranes may need to be reinserted before the density profile stabilizes.

Under non-equilibrium conditions, RBCs may advect out of the domain. When their center-of-mass crosses the outer boundary of the system, membranes are deleted from the simulation, and their momentum is added to the lost momentum. The cytosol outside the boundary is also deleted from the system, while the cytosol that remains in the domain is turned into solvent in the next iteration of the checker algorithm, which determines whether a fluid particle is located inside or outside of a cell. New cells are introduced using a procedure analogous to that employed for solvent insertion (see Sec. II B). Candidate membrane positions are tested for overlaps with other membranes; if overlaps are detected, a new position is sampled or the membrane is randomly rotated. We test for overlaps using the potential described in Eq. (17) and apply the standard USHER[48] to the position of the center-of-mass. An alternative could be using the USHER algorithm for multi-site particles,[49] but in that case, the torque on the membrane would need to be calculated, which is computationally more expensive due to the large number of interacting particles. Each inserted membrane encloses solvent particles that are subsequently turned into cytosol in the next iteration of the checker algorithm. To avoid numerical instabilities, bounce-back reflections (see Sec. III) are disabled within the insertion region. However, such insertions are possible only when the buffer hematocrit is about 20% or lower. With random insertions, rigid rotation and translation alone cannot achieve a higher hematocrit. Denser packing requires either artificial alignment of the RBCs or deformation of their membranes.

2. Growing-size insertion algorithm

We introduce a new growing-size insertion procedure that enables membrane insertions in high hematocrit simulations. The cells are inserted into the outermost layer of the simulation box at a fraction of their size, $\omega_0 \le 1$. The simulation cell is then wrapped in additional transition regions, where the membranes grow smoothly, reaching their full size in the inner layer of the buffer region. Their size is controlled by $\omega(x)$,

$$\omega(x) = \begin{cases} \omega_0, & x < x_{TR_L}, \\ \omega_0 + (1-\omega_0)\dfrac{x - x_{TR_L}}{x_{FS_L} - x_{TR_L}}, & x_{TR_L} \le x < x_{FS_L}, \\ 1, & x_{FS_L} \le x < x_{FS_R}, \\ 1 - (1-\omega_0)\dfrac{x - x_{FS_R}}{x_{TR_R} - x_{FS_R}}, & x_{FS_R} \le x < x_{TR_R}, \\ \omega_0, & x \ge x_{TR_R}, \end{cases} \tag{15}$$

which grows linearly throughout the transition region, as shown in Fig. 1. The growth is guided by rescaling the enforced area and volume as $A_0(x) = [\omega(x)]^2 A_0$ and $V_0(x) = [\omega(x)]^3 V_0$ [see Eqs. (23) and (24)].

The length of the transition layer L_{TR} needs to be high enough to allow RBCs to grow and deform smoothly. It should satisfy $L_{TR} \approx \max(u_x\tau, 2D_0)$, where u_x is a representative flow velocity along the open direction and τ is a characteristic visco-elastic growth timescale, which can be estimated by considering the velocity at which the vertices of the membrane will be expanded radially when the prescribed area and volume are increased. If their velocity is too high, the drag force due to the membrane's intrinsic viscosity η_m and the solvent's viscosity η_s will be larger than the membrane's restoring force, which is of the order of the shear modulus μ. The effective viscosity of the suspension of red blood cells scales with hematocrit $\eta_{\text{eff}} = \eta_s(1 - Ht/Ht_{\max})^{-\alpha}$,[50] where $Ht_{\max} \approx 0.75$ is the maximum packing fraction, and $\alpha \approx 2$.[51,52] The estimate of the characteristic timescale is then

$$\tau \sim \left[\frac{\eta_m + \eta_{\text{eff}} R}{\mu}\right](1 - \omega_0), \tag{16}$$

where R is the radius of the RBC. In cases where the characteristic timescale is small, the transition region is constrained to at least $2D_0$. Conversely, the buffer should be kept as short as possible, since the time delay in the transport of external conditions to the ROI is proportional to its length,[28] approximately $\tau_B \sim L_B^2 \rho m/\eta_s$. The choice of region sizes is, therefore, a compromise between these considerations. For flows with a preferred direction, the outlet side can omit insertion and transition layers entirely, as cells exit at full size, which reduces the computational cost.

Membrane insertion is performed when the search algorithm identifies a position where the interaction potential vanishes. It is probed using a novel anisotropic potential inspired by DPD and the Gay–Berne potential[53] but significantly simplified. Similar potentials were previously employed to approximate hemodynamics.[54,55] The potential defined here is purely repulsive and vanishes beyond a cut-off that depends on the mutual orientation of the two membranes α and β. It is defined as

$$V_{\alpha\beta}(r_{\alpha\beta}) = \frac{r_{\alpha\beta}^c}{2}\left[\tilde{w}(r_{\alpha\beta})\right]^2, \tag{17}$$

where

$$\sigma_{\alpha\beta} = 1 - \frac{1}{2}\left|\hat{\boldsymbol{o}}_\alpha \cdot \hat{\boldsymbol{e}}_{\alpha\beta}\right| - \frac{1}{2}\left|\hat{\boldsymbol{o}}_\beta \cdot \hat{\boldsymbol{e}}_{\alpha\beta}\right|, \tag{18}$$

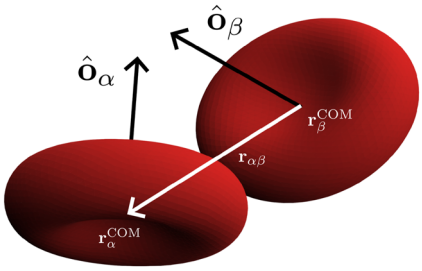

FIG. 2. Membranes α and β, their main axes, and the relative vector of their positions $\boldsymbol{r}_{\alpha\beta}$. The main axis of the RBCs is defined as the unit eigenvector of the smallest eigenvalue of the gyration tensor and is perpendicular to the biconcave surface of the RBC.

$$r_{\alpha\beta}^c = r_\parallel + \sigma_{\alpha\beta}\left(r_\perp - r_\parallel\right), \tag{19}$$

and the weight function $\tilde{w}(r)$,

$$\tilde{w}(r) = \begin{cases} 1 - r/r_{\alpha\beta}^c, & r < r_{\alpha\beta}^c, \\ 0, & r \geq r_{\alpha\beta}^c. \end{cases} \tag{20}$$

Here, $\hat{\boldsymbol{e}}_{\alpha\beta} = \boldsymbol{r}_{\alpha\beta}/r_{\alpha\beta}$, and $\boldsymbol{r}_{\alpha\beta} = \boldsymbol{r}_\alpha^{\mathrm{COM}} - \boldsymbol{r}_\beta^{\mathrm{COM}}$ is the relative displacement of the membrane's centers-of-mass (COM), while $r_\parallel$ and $r_\perp$ are the cutoff lower and upper limits and should be slightly larger than the cross section and diameter of the membrane, respectively. If $r_\parallel = r_\perp$ is set, the potential in Eqs. (17)–(20) defines an isotropic potential. The main axis $\hat{\boldsymbol{o}}_\alpha$ of membrane α is perpendicular to the biconcave surface of the RBC (Fig. 2) and is determined as the normalized eigenvector corresponding to the smallest eigenvalue of the gyration tensor.

C. Red blood cell model

The RBC membrane is represented as a triangulated surface whose evolution is governed by the bending resistance of the lipid bilayer, the shear and dilation elasticity of the spectrin cytoskeleton, and membrane viscosity. The membranes enclose the DPD cytosol. The RBC model used here has been developed and extensively validated in previous studies.[4–6] It captures single-cell dynamics such as tank-treading and tumbling in shear flow and reproduces stretching behavior observed in optical-tweezer experiments. Moreover, model parameters were calibrated using hierarchical Bayesian inference against stretching and shear-flow data.[5,6]

The energy of the membrane is split into two terms. The out-of-plane bending energy[56] depends on the local curvature of the membrane in its current configuration,

$$E_B = 2\kappa_b \oint H^2 \mathrm{d}A, \tag{21}$$

where κ_b is the bending modulus, H is the local mean curvature, and the integral is taken over the instantaneous, deformed membrane surface. In contrast, the shear energy reflects the resistance of the spectrin network to in-plane deformations and is defined relative to a stress-free reference configuration,[57]

TABLE I. RBC membrane parameters used in this study.

Parameter	Symbol	Value
Stretch modulus	K_α[6]	4.99 μN m^{-1}
Shear modulus	μ[6]	4.99 μN m^{-1}
Bending modulus	κ_b[6]	2.1×10^{-19} J
Area modulus	k_A[57]	0.5 J m^{-2}
Osmotic modulus	k_V[57]	7.23×10^5 J m^{-3}
Diameter	D_0[61]	7.82 μm
Area	A_0[61]	135 μm
Volume	V_0[61]	94 μm
Membrane viscosity	η_m[7]	$12\eta_s R_A$
Reduced volume of SFS	v[6]	0.95
Nonlinear coefficients	a_3[57]	−2
	a_4[57]	8
	b_1[57]	0.7
	b_2[6]	1.84

$$E_S = \frac{K_\alpha}{2} \oint \left(\alpha^2 + a_3\alpha^3 + a_4\alpha^4\right)\mathrm{d}A_{\mathrm{SFS}} + \mu \oint \left(\beta + b_1\alpha\beta + b_2\beta^2\right)\mathrm{d}A_{\mathrm{SFS}}, \tag{22}$$

where the integration is taken over the stress-free-shape (SFS) with a certain reduced volume v;[6] see Table I. K_α is the stretch modulus, μ is the shear modulus, α and β are the local area and shear strain invariants, respectively, and a_3, a_4, b_1, b_2 are the nonlinear elastic coefficients.[57] In addition, the area A and volume V of the red blood cell are enforced with penalization terms,

$$E_A = k_A \frac{(A - A_0)^2}{2A_0}, \tag{23}$$

$$E_V = k_V \frac{(V - V_0)^2}{2V_0}, \tag{24}$$

where k_A and k_V are the area and osmotic modulus and A_0 and V_0 are the prescribed area and volume of the RBC. The biconcave membrane is discretized into a triangulated mesh with $N_v = 2562$ vertices, each with mass m and position $\boldsymbol{r}_i$ $(i = 1, \ldots, N_v)$. The membrane energies are evaluated in discretized form following the formulations of Jülicher,[56] Bian *et al.*,[58] and Lim *et al.*,[57] as implemented in `Mirheo`.[59] Forces on the vertices are obtained as the negative gradients of the total energy with respect to their coordinates, and the vertex positions are advanced according to Newton's equations of motion. The viscous dissipation in the membrane is modeled via forces between nodes i and j that share an edge, given by

$$\boldsymbol{f}_{ij}^{visc} = -\gamma_m(\boldsymbol{v}_{ij} \cdot \hat{\boldsymbol{e}}_{ij})\hat{\boldsymbol{e}}_{ij}, \tag{25}$$

where γ_m is the membrane dissipation coefficient, related to the membrane viscosity by $\eta_m = \gamma_m\sqrt{3}/4$.

III. COMPUTATIONAL DETAILS

All simulations are performed using `Mirheo`,[59] an open-source GPU-optimized molecular dynamics simulation package. Mirheo

has already been extended for OBMD simulations of simple fluids.[36] Dimensionless units are employed throughout, with the elementary units of length U_L, mass U_M, and time U_T. The characteristic length scale is defined by the RBC sphere-equivalent area radius, $R = \sqrt{A_0/4\pi} = 6\ U_L$. The time and mass scales are derived from the solvent viscosity and thermal energy, such that the solvent viscosity $\eta_s = 26.3U_M/U_L U_T = 1.2$ mPa s and $k_B T = 0.1\ U_M U_L^2/U_T^2$ matches the thermal energy at $T = 37\,^{\circ}$C. The corresponding energy unit is $U_E = U_M U_L^2/U_T^2$.

The simulation domain size is $L_x \times L_y \times L_z = 240U_L \times 50U_L \times 50U_L$, with number density $\rho_s = \rho_c = 10\ U_L^{-3}$, where the indices s and c stand for solvent and cytosol, respectively. We set $m = 1U_M$ for both fluid and membrane particles and $r_c = 1U_L$ and $k_B T = 0.1U_E$ for all interactions. Equations of motion are integrated using the velocity-Verlet algorithm.[42,59] The time step is chosen to resolve the fastest dynamical mode in the system. Because the characteristic timescale of membrane motion is shorter than that of the solvent, the membrane is updated more frequently, and the interfacial forces are distributed over N substeps, $N = \Delta t_s/\Delta t_m$, where

$$\Delta t_s \le \frac{1}{8}\frac{h^2}{\nu} \tag{26}$$

is the global time step used to resolve the solvent, $h = \rho^{-1/3}$ is the interparticle distance, and $\nu = \eta/\rho m$ is the kinematic viscosity.[60] Similarly, for the membrane

$$\Delta t_m \le \min\left(\frac{1}{8}\frac{h_m^2}{\nu_m}, \frac{1}{4}\sqrt{\frac{h_m m}{f_{el}}}\right), \tag{27}$$

where $\nu_m = \eta_m A_0/N_v m$ is the surface kinematic viscosity, $f_{el} = \mu h + \kappa_b/h + k_A h + k_V h^2$ is the characteristic elastic force magnitude, and h_m is the average distance between the nodes of the membrane. In most cases, the limiting factor is the viscosity of the membrane. Here, the time step is $\Delta t = 0.005/\lambda\ U_T$ with $N = 135/\lambda$ substeps, where $\lambda = \eta_c/\eta_s$ is the viscosity ratio of the cytosol and the solvent.

Bounce-back reflection[59] is applied at the solvent–membrane and cytosol–membrane interfaces to prevent particle penetration across the membrane. The new velocity of the bounced particle is drawn from the Maxwellian distribution for the temperature $k_B T$, and the momentum difference is distributed among the nodes of the collided triangle, which guarantees linear but not angular momentum conservation. Bounce-back reflections are activated in the inner layer of the buffer region. Outside this layer, the membrane interacts with the solvent only through the DPD thermostat. When using the growing-size algorithm, cells are initially inserted at a reduced scale; since there is no impenetrability constraint at this stage, fluid particles can freely enter the membrane as it grows, ensuring the correct density inside. These particles are then converted into cytosol in the next iteration of the checker algorithm. If $\lambda = 1$, the checker is not needed, as the inner and outer fluids are effectively identical. To ensure no-slip boundary conditions, the interaction between the membrane and the fluid is tuned as[8]

$$\gamma_{m,\{s,c\}} = \frac{2A_0\eta_{\{s,c\}}(2s+1)(2s+2)(2s+3)(2s+4)}{3\pi\rho_{\{s,c\}}N_v r_c^4}. \tag{28}$$

The vertices of the membrane interact with the fluid only through the bounce-back reflection and the DPD thermostat. The fluid–membrane interaction is set as $a_{m,s} = a_{m,c} = 0U_E/U_L$, $\gamma_{m,s} = 3.8U_M/U_T$, and $\gamma_{m,c} = \lambda\gamma_{m,s}$. The DPD conservative forces between the fluids are set with $a_{s,s} = a_{c,s} = a_{c,c} = 10U_E/U_L$, and the thermostat with $\gamma_{s,s} = 5.3U_M/U_T$, $\gamma_{s,c} = 0U_M/U_T$, and $\gamma_{c,c} = \lambda\gamma_{s,s}$.

External OBMD forces are applied to the solvent and cytosol, and their effects are transmitted to the membranes via the DPD thermostat. Interactions between nodes belonging to distinct membranes are represented by a purely repulsive Lennard-Jones (LJ) interaction to ensure separation between neighboring RBCs. The LJ parameters are set to $\sigma_{LJ} = 0.35U_L$ and $\varepsilon_{LJ} = 1.0U_E$, with the force capped at $100U_E/U_L$. The length of the LJ interaction is chosen to correspond to the average distance between nodes on the membrane. When the growing-size insertion scheme is used, the LJ parameters become position-dependent, with σ_{LJ} scaled by $\omega(x)$ and ε_{LJ} by $\omega(x)^2$, reflecting their scaling with length. The cutoff limits for the insertion parameters are set to $r_\parallel = 10.5\omega_0 U_L$ and $r_\perp = 14.5\omega_0 U_L$. All elastic moduli used to represent the membrane are summarized in Table I. In the present study, we use the model yielding nonaggregating RBC suspensions. To model RBC aggregation, a Morse potential could alternatively be applied between cell membranes, following Fedosov *et al.*[7]

To generate the initial configuration, the cells are initially placed in the periodic simulation box with $\omega_0 = 0.5$. The membrane area, volume, thermal energy controlling membrane fluctuations, and membrane viscosity are scaled according to their respective units of length and are progressively increased, allowing the RBCs to reach their full size slowly. High hematocrit can be achieved with this approach, as the RBCs deform while growing. After the growth phase, the solvent and cytosol are added into the open box along with the full sized membranes and equilibrated with the external pressure p_{xx} determined from the DPD equation of state, Eq. (8), to establish a flat density profile (Fig. 4). Finally, shear flow is imposed by applying equally opposing forces on each end of the buffers, Eq. (10). After some time, a steady-state linear velocity profile $v_y(x)$ is established along the x-axis. The shear rate is measured as the slope of

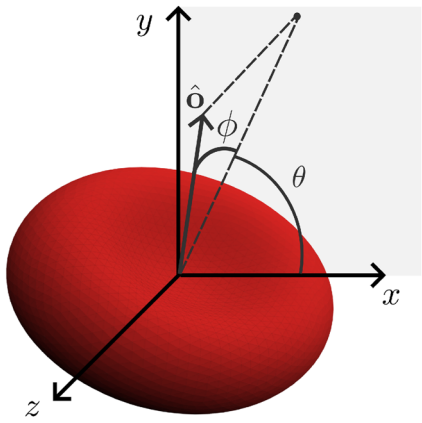

FIG. 3. Schematic of the orientation angles, where the RBC orientation is represented by $\hat{\mathbf{o}}$, θ is the in-plane orientation, and ϕ measures the out-of-plane tilt. Together, θ and ϕ define the full orientation of the cell in shear flow.

the tangential velocity across the open direction $\dot{\gamma} = \mathrm{d}v_y/\mathrm{d}x$. Ultimately, the viscosity is determined as $\eta = p_{xy}/\dot{\gamma}$. The orientation of the RBCs in shear flow is evaluated using two angles: the in-plane inclination θ, defined in the xy-plane relative to the flow-gradient direction (x-axis), and the out-of-plane inclination ϕ, defined as the tilt relative to the xy-plane, as shown on Fig. 3. Due to the symmetry of the RBC, $\hat{\mathbf{o}} = -\hat{\mathbf{o}}$, the in-plane inclination angle θ has a 180° symmetry, meaning θ and $\theta \pm 180°$ correspond to the same physical orientation.

IV. RESULTS

In OBMD, the density profile along the open direction depends on the choice of the distribution function, Eq. (13).[45] A key requirement in equilibrium is that the density profile remains flat across the buffer-ROI boundary in order to avoid spurious currents at the interface.[29,45] For non-equilibrium conditions, such as time-dependent pressure gradients, the main requirement is a smooth and continuous density transition. In our simulations of equilibrium, the density profile within the ROI is flat for both the solvent and the cytosol, with no artificial accumulation at the ROI–buffer interface, and it decreases smoothly toward the open boundary; see Fig. 4. The cytosol number density $\rho_c = 4.5\ U_L^{-3}$ corresponds to a hematocrit of 45%. Similar density profiles are obtained for all simulated hematocrits. They remain stable throughout our simulations, which were run up to 2.8 s. By varying the external pressure p_{xx}, the EOS is computed; see Fig. 4. The steady-state densities obtained with OBMD are in excellent agreement with the predicted EOS in Eq. (8), both for the single-size ($\omega_0 = 1$) and the growing-size ($\omega_0 = 0.8$) setups, demonstrating that the framework maintains equilibrium across a range of densities. The match with the predicted EOS, which is determined from the fluid's ideal-gas and virial contributions to the pressure, reflects the fact that the short-range membrane–membrane interactions and the bounce reflections contribute negligibly to the bulk pressure in the simulated range. At higher pressures, increased membrane–membrane repulsions and stronger bounce-back reflections could become more significant and might lead to deviations from the fluid EOS.

The efficiency of the membrane insertion algorithm determines how densely RBCs can be packed in the buffer regions and is probed by placing the RBC membranes into a periodic box until no additional insertion positions are available. First, insertions without scaling the membranes ($\omega_0 = 1$) and with an isotropic potential set by $r_\parallel = r_\perp$, see Eqs. (17)–(20), are performed. The volumetric fraction achieved is only about 15%, which is notably low. To improve packing efficiency, we introduce an anisotropic potential by setting $r_\parallel < r_\perp$, therefore accounting for the relative orientations of the RBCs. This modification increases the packing fraction to ~22%. As this is still relatively low, we further enhance the algorithm by inserting membranes at a reduced size and then evaluating the hematocrit corresponding to their fully grown state. The growing-size setup does not aim to reproduce the properties of RBC suspensions in the buffer but is used only as a practical method for inserting cells into dense suspensions. As expected, the packing fraction increases rapidly with decreasing initial scale, following a $\sim 1/\omega_0^3$ dependence, as shown in Fig. 5. This is a substantial improvement over the straightforward random full-scale insertion. In this study, we use

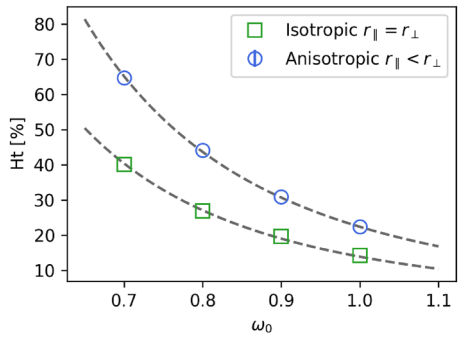

FIG. 5. Volumetric concentration the insertion algorithm can achieve depending on the length fraction ω_0 of the inserted membrane with an isotropic (green squares) and anisotropic potential (blue circles); see Eq. (17). The dashed lines are $\sim 1/\omega_0^3$ fits to the data. Because of the cubed dependence, even a small decrease in ω_0 can increase the packing fraction greatly.

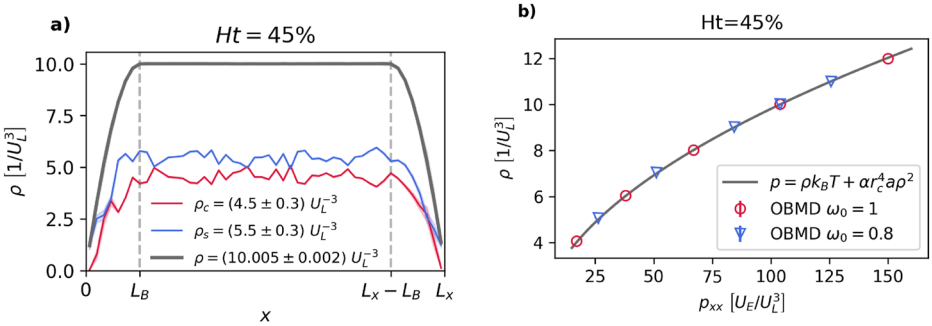

FIG. 4. (a) Number density profile throughout the simulation box in the open direction for $Ht = 45\%$ and $\omega_0 = 1$. The density profile is flat in the region of interest for both cytosol (red) and solvent (blue) and their sum (gray) and is decreasing from the buffer-ROI boundary outwards. The shaded regions show the standard deviations of the results. (b) The equation of state computed with single-size OBMD $\omega_0 = 1$ (red circles) and growing-size $\omega_0 = 0.8$ (blue triangles) compared with the quadratic equation of state for DPD (gray line). The standard deviations of the simulation results are smaller than the marker size.

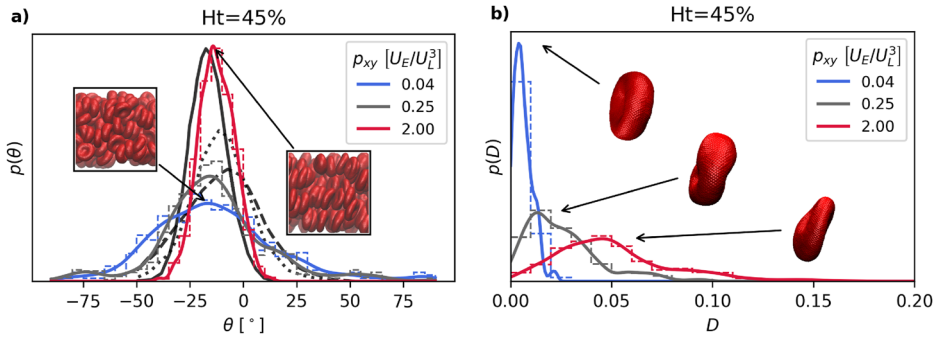

FIG. 6. Distribution of inclination angles (a) and deformation (b) in a red blood cell suspension with $Ht = 45\%$ for a few values of the applied shear stress p_{xy} corresponding to shear rates of $\dot{\gamma} = 1\ s^{-1}$ (blue), $8\ s^{-1}$ (gray), and $119\ s^{-1}$ (red) with $\omega_0 = 1$. The red blood cells align and deform in strong shear flow. The binned probabilities (colored dashed lines) are overlaid with a Gaussian kernel density estimate (colored full lines). In panel (a), we compare our results to Ref. 15 (black) at $Ht = 55\%$, with shear rates of $\dot{\gamma} = 1\ s^{-1}$ (dashed), $12\ s^{-1}$ (dotted), and $117\ s^{-1}$ (solid). The distributions are normalized to the same peak for visual comparison.

$\omega_0 = 0.8$, which enables efficient packing at high hematocrits. Lower values of ω_0 can also be used if a higher hematocrit is required; however, the transition region needs to be sufficiently large to allow smooth membrane growth.

Turning now to bulk rheological properties, the shear response of RBC suspensions under shear stress is examined. By comparing the distributions of inclination angles and deformation indices for three representative shear stresses, we find that the suspension microstructure changes under different shear rates; see Fig. 6. The inclination angle θ is defined as the angle between the main axis $\hat{\boldsymbol{o}}$ of the RBC (computed as in Fig. 3) in the xy-plane and the flow-gradient direction (x). The deformation of the cells is quantified using the Taylor deformation index, $D = (\hat{a} - \hat{b})/(\hat{a} + \hat{b})$, where $\hat{a} = a/a_0$ and $\hat{b} = b/b_0$ are the major and minor semi-axes normalized by the undeformed RBC dimensions.[15,62,63] At low shear rates, cells tumble and display a broad distribution of orientations. As the shear rate increases, the cells rearrange themselves to reduce the drag they are producing relative to the shear flow direction. The distribution of θ then shifts toward alignment with the flow, exhibiting collective orientational ordering. In addition, the shear stress is competing with the elastic deformability of the cells: at low shear, cells deform intermittently, whereas when the shear stress is high enough, the cells deform significantly by elongating along the flow direction. These observations are consistent with previous experimental and computational studies.[7,15,63] We compare our distributions of inclination angles to those reported in Ref. 15 and observe a similar narrowing of the distribution at high shear, with cells aligning to approximately the same angle relative to the flow. At low shear, the distributions depend on the initial dispersion of inclination angles in the suspension.

To quantify the narrowing of the orientation distribution, we compute the nematic order parameter of the suspension, which describes the orientational order of molecules in a suspension. The order parameter S and the director, representing the mean orientation, are defined as the largest eigenvalue of the nematic tensor $Q_{ij} = \langle 3o_i o_j - \delta_{ij} \rangle/2$ and its eigenvector, respectively.[64] Here, $\hat{\mathbf{o}}$ is the RBC main axis (see Fig. 2), and the tensor is obtained as the average over time and cells in the region of interest. The order parameter can, in principle, range from $-1/2$ to 1, with $S = 1$ corresponding to perfect alignment along the director, $S = 0$ to complete disorder, and $S = -1/2$ to perfect alignment perpendicular to the director, although this latter configuration is rare.[65] The simulated

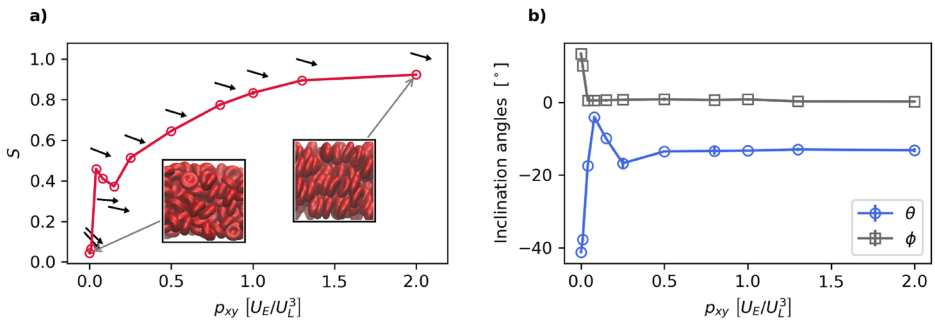

FIG. 7. (a) Nematic order parameter S as a function of shear stress p_{xy}. The black arrows are the projections of the director on the xy plane at each shear stress. The standard deviations of the data points are smaller than the symbol size. (b) The orientation of the director, where θ is the in-plane (blue circles) and ϕ is the out-of-plane (gray squares) inclination angle. Error bars indicate the standard deviation of the director angles over time.

shear-stress range spans a wide interval of orientational order, as shown in Fig. 7. The degree of ordering depends strongly on the imposed shear stress: S increases from a small, non-zero value in the absence of shear, which reflects the alignment imposed by the dense packing fraction, to nearly unity at high shear. At low shear stresses, the RBCs tumble, lowering the orientational order due to rotation of the main axes.[63] This appears as the kink around $p_{xy} = 0.05\ U_E/U_L^3$ in Fig. 7 and arises from the tumbling motion of RBCs, which manifests as an oscillating nematic order parameter $S(t)$. S shown here is averaged over the last 0.05 s of the simulation, after the shear-rate has reached its steady state. At lower shear rates, these oscillations are more pronounced, causing the observed kink. As the shear rate increases, the oscillation frequency rises while the amplitude decreases. The shear-induced flow alignment of RBCs resembles the flow-alignment of elongated or disk-like particles under shear.[66] However, the oscillatory behavior of the order parameter indicates a more complex dynamics, which is a part of our future work.

At higher shear stresses, S rises steadily with increasing shear as the RBCs settle into tank-treading with a stable orientation. A plateau is reached at a very high orientational order around $S = 0.93$, indicating strong alignment with the director. Perfect alignment is not expected as the main axes of the RBCs wobble with fluctuating stresses. The inclination of the director is described in terms of the in-plane θ and out-of-plane ϕ inclination (see Fig. 3). At low values of the nematic order parameter S, the director is mathematically well-defined but physically somewhat arbitrary because the orientational distribution is nearly isotropic. Therefore, θ and ϕ, as shown in Fig. 7, should be interpreted together with the magnitude of S. As the shear rate increases from the low to intermediate regime, the in-plane director angle starts to settle into a preferred orientation. Interestingly, the small out-of-plane component present at zero shear vanishes at very low shear, meaning that the RBCs rapidly align with the flow plane. In steady shear, the orientation of the director is stable, as indicated by the small standard deviations in the angle measurements in Fig. 7.

The collective ordering of RBCs strongly influences macroscopic properties, as shown in the viscosity measurements summarized in Fig. 8. These measurements align closely with experimental data from Chien *et al.*[2,3] for Ringer suspensions, where fibrinogen is removed to prevent cell aggregation. The simulated shear rates span 0.2–120 s^{-1}, covering the main shear-thinning regime for RBC suspensions. Simulations reproduce the expected behavior: at low shear rates, the viscosity is high due to the random arrangement of cells, while at high shear rates, the cells align, lowering flow resistance. As expected, viscosity increases with hematocrit due to the higher cell volume fraction, which raises the collective resistance to flow. An important parameter in hemorheological studies is the viscosity ratio of the cytosol and the solvent $\lambda = \eta_c/\eta_s$, which is often reported as $\lambda \approx 5$ under physiological conditions, but recent experimental measurements indicate that it may be higher than previously assumed, with mean values near $\lambda \approx 10$.[67] This parameter determines the dynamical modes and morphological transitions of RBCs in shear flow.[68–70] An advantage of the DPD method is that the viscosities of the two fluids can be tuned independently. Since the simulation time step is limited by the largest viscosity in the system [Eq. (26)], it is most efficient to set $\lambda = 1$.[7] This is because higher viscosity ratios reduce the time step proportionally, increasing the computational cost. Importantly, simulations with $\lambda = 1$ reproduce experimental relative viscosities η/η_s very well (Fig. 8), while $\lambda = 5$ slightly overestimates the viscosity. Similar studies have reported good agreement with experiments using $\lambda = 1$[7,15] and a somewhat higher viscosity with $\lambda = 5$.[68] However, high-hematocrit rheological studies are rare, as DPD simulations employing $\lambda > 1$ are most often restricted to single-cell dynamics.[6] The discrepancy observed for $\lambda = 5$ may reflect the fact that the model was primarily calibrated against single-cell mechanical properties, rather than the viscosity of dense suspensions at high hematocrit when enforcing a physical viscosity contrast. Nevertheless, the overall trend of viscosity vs

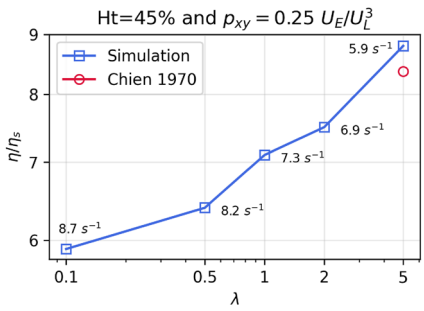

FIG. 9. Relative viscosity vs the ratio of inner and outer viscosity for $\omega_0 = 1$. Here, the solvent viscosity is constant, and the cytosol viscosity is varied. The red data point is the closest experimental value from Ref. 3.

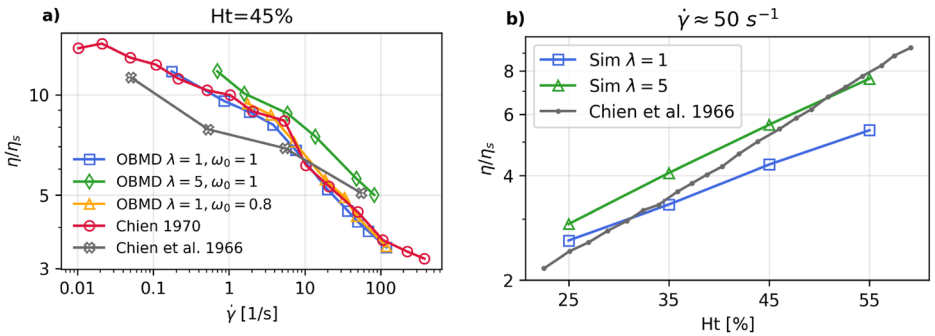

FIG. 8. Shear-thinning and viscosity increase with hematocrit—simulation results compared with experiments from Refs. 2 and 3. (a) Relative viscosity measurements compared with experiments over a wide range of shear rates. (b) Relative viscosity vs hematocrit for ~50 s^{-1} with $\omega_0 = 1$.

shear rate is captured, and the magnitude of the difference is small relative to the broad physiological range. Overall, we conclude that setting $\lambda = 1$ is optimal to capture the bulk rheological behavior for studies where the precise ratio of viscosities is not critical. As the shear stress is kept constant, the relative viscosity increases noticeably with λ, as illustrated in Fig. 9. The observed increase in viscosity with λ is significant and reflects the greater dissipation in the more viscous RBCs rather than the small differences in steady-state shear rate.

V. CONCLUSIONS

We extended the OBMD applicability to RBC suspensions and validated its ability to sustain equilibrium and reproduce known hemorheological behavior. The simulations recover key bulk properties under equilibrium by maintaining uniform density in the region of interest and matching the theoretical equation of state. The framework captures the experimental rheological response, including shear-thinning with apparent viscosities closely aligned with experimental measurements across a wide range of shear stresses and the expected rise in viscosity with hematocrit. A major novel feature of the framework is the robust insertion of RBC membranes at high hematocrits using an anisotropic potential combined with a reduced size at insertion, allowing dense packing without disrupting hemorheological properties in the bulk. This approach significantly improves packing efficiency, increasing the volumetric fraction from about 15% for the full-size insertion with an isotropic potential to ~45% when the insertion scale is set to $\omega_0 = 0.8$. An even higher hematocrit can be achieved by further decreasing the membrane's size at insertion. This is essential when studying blood rheology in physiological and pathological conditions, such as in patients with polycythemia, where elevated hematocrit strongly affects flow properties.

This study is a first step toward exploring the behavior of therapeutic agents in physiologically relevant suspensions, focusing in particular on how RBC suspensions modify the acoustic field and influence the acoustic response of agents such as microbubbles and gas vesicles. Recent DPD models[71] provide compatible representations of such agents and offer a natural extension to study their interactions with blood. Beyond acoustically driven flows, the OBMD framework is applicable to a wide range of non-equilibrium blood flow problems where periodic boundaries are inadequate, including pressure-driven flows, transient start-up and relaxation phenomena, and systems with hematocrit gradients along the flow direction or time-dependent inflow conditions.[72,73] The method also enables studies of flow-induced RBC deformation and the formation of cell-free layers.[74] More generally, the approach can be extended to other dense suspensions of deformable objects, such as capsules, vesicles, or soft colloids, where controlled exchange with the surroundings is essential.

ACKNOWLEDGMENTS

The authors acknowledge the financial support under the ERC Advanced Grant (Grant No. 885155) from the European Research Council.

AUTHOR DECLARATIONS

Conflict of Interest

The authors have no conflicts to disclose.

Author Contributions

Maša Lah: Conceptualization (equal); Investigation (lead); Methodology (equal); Software (lead); Validation (lead); Writing – original draft (lead); Writing – review & editing (equal). **Tilen Potisk**: Conceptualization (equal); Investigation (equal); Methodology (equal); Supervision (equal); Validation (equal); Writing – original draft (equal); Writing – review & editing (equal). **Matej Praprotnik**: Conceptualization (lead); Funding acquisition (lead); Investigation (equal); Methodology (equal); Supervision (equal); Validation (equal); Writing – original draft (equal); Writing – review & editing (equal).

DATA AVAILABILITY

The data that support the findings of this study are available from the corresponding author upon reasonable request.

REFERENCES

[1] J. E. Hall and A. C. Guyton, *Guyton and Hall Textbook of Medical Physiology*, 14th ed. (Elsevier, 2021).
[2] S. Chien, S. Usami, H. M. Taylor, J. L. Lundberg, and M. I. Gregersen, "Effects of hematocrit and plasma proteins on human blood rheology at low shear rates," J. Appl. Physiol. **21**, 81–87 (1966).
[3] S. Chien, "Shear dependence of effective cell volume as a determinant of blood viscosity," Science **168**, 977–979 (1970).
[4] A. Economides, L. Amoudruz, S. Litvinov, D. Alexeev, S. Nizzero, P. E. Hadjidoukas, D. Rossinelli, and P. Koumoutsakos, "Towards the virtual rheometer: High performance computing for the red blood cell microstructure," in *Proceedings of the Platform for Advanced Scientific Computing Conference* (Association for Computing Machinery, 2017), pp. 1–13.
[5] A. Economides, G. Arampatzis, D. Alexeev, S. Litvinov, L. Amoudruz, L. Kulakova, C. Papadimitriou, and P. Koumoutsakos, "Hierarchical Bayesian uncertainty quantification for a model of the red blood cell," Phys. Rev. Appl. **15**, 034062 (2021).
[6] L. Amoudruz, A. Economides, G. Arampatzis, and P. Koumoutsakos, "The stress-free state of human erythrocytes: Data-driven inference of a transferable RBC model," Biophys. J. **122**, 1517–1525 (2023).
[7] D. A. Fedosov, W. Pan, B. Caswell, G. Gompper, and G. E. Karniadakis, "Predicting human blood viscosity in silico," Proc. Natl. Acad. Sci. U. S. A. **108**, 11772–11777 (2011).
[8] D. A. Fedosov, B. Caswell, and G. E. Karniadakis, "A multiscale red blood cell model with accurate mechanics, rheology, and dynamics," Biophys. J. **98**, 2215–2225 (2010).
[9] I. V. Pivkin and G. E. Karniadakis, "Accurate coarse-grained modeling of red blood cells," Phys. Rev. Lett. **101**, 118105 (2008).
[10] D. A. Fedosov, B. Caswell, and G. E. Karniadakis, "Systematic coarse-graining of spectrin-level red blood cell models," Comput. Methods Appl. Mech. Eng. **199**, 1937–1948 (2010).
[11] D. A. Fedosov, H. Lei, B. Caswell, S. Suresh, and G. E. Karniadakis, "Multiscale modeling of red blood cell mechanics and blood flow in malaria," PLoS Comput. Biol. **7**, e1002270 (2011).
[12] K. Müller, D. A. Fedosov, and G. Gompper, "Understanding particle margination in blood flow—A step toward optimized drug delivery systems," Med. Eng. Phys. **38**, 2–10 (2016).

[13]T. Ye, N. Phan-Thien, B. C. Khoo, and C. T. Lim, "Dissipative particle dynamics simulations of deformation and aggregation of healthy and diseased red blood cells in a tube flow," Phys. Fluids **26**, 111902 (2014).
[14]T. Ye, N. Phan-Thien, B. C. Khoo, and C. T. Lim, "A file of red blood cells in tube flow: A three-dimensional numerical study," J. Appl. Phys. **116**, 124703 (2014).
[15]H. Krüger, *Computer Simulation Study of Collective Phenomena in Dense Suspensions of Red Blood Cells Under Shear* (Springer Science & Business Media, 2012).
[16]F. Guglietta, M. Behr, L. Biferale, G. Falcucci, and M. Sbragaglia, "Lattice Boltzmann simulations on the tumbling to tank-treading transition: Effects of membrane viscosity," Philos. Trans. R. Soc., A **379**, 20200395 (2021).
[17]X. Shi, G. Lin, J. Zou, and D. A. Fedosov, "A lattice Boltzmann fictitious domain method for modeling red blood cell deformation and multiple-cell hydrodynamic interactions in flow," Int. J. Numer. Methods Fluids **72**, 895–911 (2013).
[18]S. M. Hosseini and J. J. Feng, "A particle-based model for the transport of erythrocytes in capillaries," Chem. Eng. Sci. **64**, 4488–4497 (2009).
[19]S. M. Hosseini and J. J. Feng, "How malaria parasites reduce the deformability of infected red blood cells," Biophys. J. **103**, 1–10 (2012).
[20]D. A. Fedosov, M. Peltomäki, and G. Gompper, "Deformation and dynamics of red blood cells in flow through cylindrical microchannels," Soft Matter **10**, 4258–4267 (2014).
[21]H. Noguchi and G. Gompper, "Shape transitions of fluid vesicles and red blood cells in capillary flows," Proc. Natl. Acad. Sci. U. S. A. **102**, 14159–14164 (2005).
[22]D. E. Discher, D. H. Boal, and S. K. Boey, "Simulations of the erythrocyte cytoskeleton at large deformation. II. Micropipette aspiration," Biophys. J. **75**, 1584–1597 (1998).
[23]M. M. Dupin, I. Halliday, C. M. Care, L. Alboul, and L. L. Munn, "Modeling the flow of dense suspensions of deformable particles in three dimensions," Phys. Rev. E **75**, 066707 (2007).
[24]A. W. Lees and S. F. Edwards, "The computer study of transport processes under extreme conditions," J. Phys. C: Solid State Phys. **5**, 1921 (1972).
[25]E. G. Flekkøy, G. Wagner, and J. Feder, "Hybrid model for combined particle and continuum dynamics," Europhys. Lett. **52**, 271 (2000).
[26]E. G. Flekkøy, R. Delgado-Buscalioni, and P. V. Coveney, "Flux boundary conditions in particle simulations," Phys. Rev. E **72**, 026703 (2005).
[27]R. Delgado-Buscalioni and P. V. Coveney, "Continuum-particle hybrid coupling for mass, momentum, and energy transfers in unsteady fluid flow," Phys. Rev. E **67**, 046704 (2003).
[28]R. Delgado-Buscalioni, K. Kremer, and M. Praprotnik, "Concurrent triple-scale simulation of molecular liquids," J. Chem. Phys. **128**, 114110 (2008).
[29]R. Delgado-Buscalioni and G. De Fabritiis, "Embedding molecular dynamics within fluctuating hydrodynamics in multiscale simulations of liquids," Phys. Rev. E **76**, 036709 (2007).
[30]D. A. Fedosov and G. E. Karniadakis, "Triple-decker: Interfacing atomistic–mesoscopic–continuum flow regimes," J. Comput. Phys. **228**, 1157–1171 (2009).
[31]K. Lykov, X. Li, H. Lei, I. V. Pivkin, and G. E. Karniadakis, "Inflow/outflow boundary conditions for particle-based blood flow simulations: Application to arterial bifurcations and trees," PLoS Comput. Biol. **11**, e1004410 (2015).
[32]H. Lei, D. A. Fedosov, and G. E. Karniadakis, "Time-dependent and outflow boundary conditions for dissipative particle dynamics," J. Comput. Phys. **230**, 3765–3779 (2011).
[33]R. Delgado-Buscalioni, J. Sablić, and M. Praprotnik, "Open boundary molecular dynamics," Eur. Phys. J.: Spec. Top. **224**, 2331–2349 (2015).
[34]J. Sablić, M. Praprotnik, and R. Delgado-Buscalioni, "Open boundary molecular dynamics of sheared star-polymer melts," Soft Matter **12**, 2416–2439 (2016).
[35]P. Papež and M. Praprotnik, "Dissipative particle dynamics simulation of ultrasound propagation through liquid water," J. Chem. Theory Comput. **18**, 1227–1240 (2022).
[36]M. Lah, N. Ntarakas, T. Potisk, P. Papež, and M. Praprotnik, "Open-boundary molecular dynamics of ultrasound using supramolecular water models," J. Chem. Phys. **162**, 024103 (2025).
[37]P. Papež, F. Merzel, and M. Praprotnik, "Sub-THz acoustic excitation of protein motion," J. Chem. Phys. **159**, 135101 (2023).
[38]R. Delgado-Buscalioni, "Tools for multiscale simulation of liquids using open molecular dynamics," in *Numerical Analysis of Multiscale Computations: Proceedings of a Winter Workshop at the Banff International Research Station 2009* (Springer, 2011), pp. 145–166.
[39]M. K. Borg, D. A. Lockerby, and J. M. Reese, "The FADE mass-stat: A technique for inserting or deleting particles in molecular dynamics simulations," J. Chem. Phys. **140**, 074110 (2014).
[40]B. D. Lubachevsky and F. H. Stillinger, "Geometric properties of random disk packings," J. Stat. Phys. **60**, 561–583 (1990).
[41]A. R. Kansal, S. Torquato, and F. H. Stillinger, "Computer generation of dense polydisperse sphere packings," J. Chem. Phys. **117**, 8212–8218 (2002).
[42]R. D. Groot and P. B. Warren, "Dissipative particle dynamics: Bridging the gap between atomistic and mesoscopic simulation," J. Chem. Phys. **107**, 4423–4435 (1997).
[43]J. Wang, Y. Han, Z. Xu, X. Yang, S. Ramakrishna, and Y. Liu, "Dissipative particle dynamics simulation: A review on investigating mesoscale properties of polymer systems," Macromol. Mater. Eng. **306**, 2000724 (2021).
[44]K. P. Santo and A. V. Neimark, "Dissipative particle dynamics simulations in colloid and interface science: A review," Adv. Colloid Interface Sci. **298**, 102545 (2021).
[45]R. Delgado-Buscalioni, "Tools for multiscale simulation of liquids using open molecular dynamics," in *Numerical Analysis of Multiscale Computations: Proceedings of a Winter Workshop at the Banff International Research Station, 2009*, *Lecture Notes in Computational Science and Engineering*, edited by B. Engquist, O. Runborg, and Y. R. Tsai (Springer, 2011), Vol. 82, pp. 145–166.
[46]J. Zavadlav, J. Sablić, R. Podgornik, and M. Praprotnik, "Open-boundary molecular dynamics of a dna molecule in a hybrid explicit/implicit salt solution," Biophys. J. **114**, 2352–2362 (2018).
[47]J. H. Walther, M. Praprotnik, E. M. Kotsalis, and P. Koumoutsakos, "Multiscale simulation of water flow past a C_{540} fullerene," J. Comput. Phys. **231**, 2677–2681 (2012).
[48]R. Delgado-Buscalioni and P. V. Coveney, "USHER: An algorithm for particle insertion in dense fluids," J. Chem. Phys. **119**, 978–987 (2003).
[49]G. De Fabritiis, R. Delgado-Buscalioni, and P. V. Coveney, "Energy controlled insertion of polar molecules in dense fluids," J. Chem. Phys. **121**, 12139–12142 (2004).
[50]I. M. Krieger and T. J. Dougherty, "A mechanism for non-Newtonian flow in suspensions of rigid spheres," Trans. Soc. Rheol. **3**, 137–152 (1959).
[51]S. Chien, S. Usami, R. J. Dellenback, and M. I. Gregersen, "Shear-dependent deformation of erythrocytes in rheology of human blood," Am. J. Physiol. **219**, 136–142 (1970).
[52]A. Bohiniková, I. Jančigová, and I. Cimrák, "Modeling red blood cell viscosity contrast using inner soft particle suspension," Micromachines **12**, 974 (2021).
[53]D. J. Cleaver, C. M. Care, M. P. Allen, and M. P. Neal, "Extension and generalization of the Gay-Berne potential," Phys. Rev. E **54**, 559 (1996).
[54]F. Janoschek, F. Toschi, and J. Harting, "Simplified particulate model for coarse-grained hemodynamics simulations," Phys. Rev. E **82**, 056710 (2010).
[55]F. Janoschek, F. Mancini, J. Harting, and F. Toschi, "Rotational behaviour of red blood cells in suspension: A mesoscale simulation study," Philos. Trans. R. Soc., A **369**, 2337–2344 (2011).
[56]F. Jülicher, "The morphology of vesicles of higher topological genus: Conformal degeneracy and conformal modes," Z. Phys. **6**, 1797–1824 (1996).
[57]H. G. Lim, M. Wortis, and R. Mukhopadhyay, "Red blood cell shapes and shape transformations: Newtonian mechanics of a composite membrane," in *Soft Matter: Lipid Bilayers and Red Blood Cells*, edited by G. Gompper and M. Schick (Wiley-VCH, Weinheim, 2009), Vol. 4, pp. 83–139.
[58]X. Bian, S. Litvinov, and P. Koumoutsakos, "Bending models of lipid bilayer membranes: Spontaneous curvature and area-difference elasticity," Comput. Methods Appl. Mech. Eng. **359**, 112758 (2020).
[59]D. Alexeev, L. Amoudruz, S. Litvinov, and P. Koumoutsakos, "Mirheo: High-performance mesoscale simulations for microfluidics," Comput. Phys. Commun. **254**, 107298 (2020).
[60]J. P. Morris, P. J. Fox, and Y. Zhu, "Modeling low Reynolds number incompressible flows using SPH," J. Comput. Phys. **136**, 214–226 (1997).

[61] E. Evans and Y.-C. Fung, "Improved measurements of the erythrocyte geometry," Microvasc. Res. **4**, 335–347 (1972).
[62] G. I. Taylor, "The formation of emulsions in definable fields of flow," Proc. R. Soc. London, Ser. A **146**, 501–523 (1934).
[63] T. Krüger, M. Gross, D. Raabe, and F. Varnik, "Crossover from tumbling to tank-treading-like motion in dense simulated suspensions of red blood cells," Soft Matter **9**, 9008–9015 (2013).
[64] P. G. De Gennes, "Short range order effects in the isotropic phase of nematics and cholesterics," Mol. Cryst. Liq. Cryst. **12**, 193–214 (1971).
[65] S. Kumar, *Liquid Crystals: Experimental Study of Physical Properties and Phase Transitions* (Cambridge University Press, 2001).
[66] T. M. Fischer and R. Korzeniewski, "Angle of inclination of tank-treading red cells: Dependence on shear rate and suspending medium," Biophys. J. **108**, 1352–1360 (2015).
[67] T. John, K. Kretsch, F. M. Maurer, S. M. Recktenwald, L. Kaestner, and C. Wagner, "Viscosity and density measurements on the cytosol of human red blood cells," Biophys. J. **124**, 2668–2676 (2025).
[68] L. Lanotte, J. Mauer, S. Mendez, D. A. Fedosov, J.-M. Fromental, V. Claveria, F. Nicoud, G. Gompper, and M. Abkarian, "Red cells' dynamic morphologies govern blood shear thinning under microcirculatory flow conditions," Proc. Natl. Acad. Sci. U. S. A. **113**, 13289–13294 (2016).
[69] J. Mauer, S. Mendez, L. Lanotte, F. Nicoud, M. Abkarian, G. Gompper, and D. A. Fedosov, "Flow-induced transitions of red blood cell shapes under shear," Phys. Rev. Lett. **121**, 118103 (2018).
[70] A. K. Dasanna, J. Mauer, G. Gompper, and D. A. Fedosov, "Importance of viscosity contrast for the motion of erythrocytes in microcapillaries," Front. Phys. **9**, 666913 (2021).
[71] N. Ntarakas, M. Lah, D. Svenšek, T. Potisk, and M. Praprotnik, "Dissipative particle dynamics models of encapsulated microbubbles and nanoscale gas vesicles for biomedical ultrasound simulations," ACS Appl. Nano Mater. **8**, 16053–16070 (2025).
[72] B. M. Hill and C. R. Leonardi, "Lattice Boltzmann simulation of transient blood flow in arterial geometries using a regularised, viscoplastic and shear-thinning fluid," Int. J. Numer. Methods Biomed. Eng. **37**, e3456 (2021).
[73] S. M. Recktenwald, K. Graessel, Y. Rashidi, J. N. Steuer, T. John, S. Gekle, and C. Wagner, "Cell-free layer of red blood cells in a constricted microfluidic channel under steady and time-dependent flow conditions," Phys. Rev. Fluids **8**, 074202 (2023).
[74] B.-J. Lai, L.-T. Zhu, Z. Chen, B. Ouyang, and Z.-H. Luo, "Review on blood flow dynamics in lab-on-a-chip systems: An engineering perspective," Chem Bio Eng. **1**, 26–43 (2024).